Research Article

In Situ Forming MnFe$_2$O$_4$/D201 Magnetic Composite Adsorbents for High Selectivity Adsorption and Deep Treatment of As(V) from Wastewater

Shaopeng Zhang [ID],[1,2] Jie Ding,[1] Dayong Tian,[1] Feifei Liu,[1] Qiaoling Li,[1] and Minghua Lu [ID][2]

[1]*College of Chemical and Environmental Engineering, Anyang Institute of Technology, Anyang, 455000 Henan, China*
[2]*College of Chemistry and Chemical Engineering, Henan University, Kaifeng, 475004 Henan, China*

Correspondence should be addressed to Shaopeng Zhang; 20200035@ayit.edu.cn and Minghua Lu; mhlu@henu.edu.cn

A new magnetic adsorbent, namely, MnFe$_2$O$_4$/D201, with deep-treatment ability and high selectivity adsorption for As(V) was prepared. According to isotherm adsorption and kinetics, As(V) adsorption is primarily used for chemical bonding throughout the single-layer adsorbing process. The maximum As(V) adsorption capacity of MnFe$_2$O$_4$/D201 can reach 35.8 mg/g at pH 3. MnFe$_2$O$_4$/D201 also exhibits higher selectivity adsorption against Cl$^-$, NO$_3$$^-$, SO$_4$$^{2-}$, and PO$_4$$^{3-}$. According to the thermodynamic results, the adsorption process was spontaneous and endothermic. The adsorption capacity is maintained at 81% of the initial after ten adsorption-desorption cycles. As(V) concentrations ranging from 1 mg/L to 10 μg/L can be treated in fixed-bed column experiments. The effectual cure volume of As(V) reaches 1332 BV (26.64 L). The removal mechanism primarily comprises electrostatic attraction and complexation.

1. Introduction

Arsenic, as a metalloid material with high toxicity, is widely available and is a significant synthetic material in the fields of industry, agriculture, semiconductor substances, and so on [1]. Because of the increasing demand for As, the issue of As-containing wastewater is also on the rise, causing severe water and soil pollution. For this reason, the World Health Organization (WHO) has set the maximum As concentration in drinking water at 10 μg/L to reduce As poisoning [2]. For a long time, approximately 150 million people in over 70 countries consumed As-contaminated water consumption, resulting in long-term damage from arsenic pollution [3]. As(V) is a class I carcinogenic element, and drinking water containing a significant amount of As poses severe health risks, including cancers and neurological diseases [4]. Therefore, it is critical and urgent to find an effective technology for reducing As(V) concentration.

Many strategies have been learnt and used in oxyanion-polluted wastewater treatment, including membrane separation, adsorption, biological treatment, chemical precipitation, and ion exchange [5]. Among various strategies, adsorption technology has attracted significant attention because of its unique treatment effect, broad application scope, important reusability, and other advantages. Therefore, many adsorbents have been proposed to treat As(V)-contaminated drinking water, including cellulose, chitosan, iron oxides, clays, zeolites, alginate, and biochar [6]. In recent years, nanomaterials have piqued interest as adsorbents because of their exceptional properties [7]. Although nanomaterials exhibit good adsorption efficiency, it is not easy to recollect the used adsorbents after pollutant adsorption [8]. The fast development of magnetized nanotechnology has provided novel possibilities for promoting the water treatment process [9]. Among these adsorbents [10], MnFe$_2$O$_4$ is one of the most essential chosen and worthy ecofriendly materials and has piqued considerable interest because of its easy synthesis, convenient recyclability, and biocompatibility. MnFe$_2$O$_4$ is extensively used in As(V) remediation because of its excellent sorption capacity and

availability. Nevertheless, $MnFe_2O_4$ is inclined to self-aggregate because of its large specific surface area and minor scales, degrading the adsorption efficiencies [11].

In addition, considering the problems of aggregation and recovery difficulty of the nanomaterial $MnFe_2O_4$, supporting materials (such as activated carbon, carbon nanotubes, resins, and graphene) are employed to provide support to enable nanoadsorbent to be well recycled through a facile "filtrating-washing" process [12], thereby overcoming the disadvantages of the traditional powdered $MnFe_2O_4$ nanomaterial. Moreover, their specific surface area and dispersibility can be improved, thereby improving their reactivity [13].

Among these supporting substances, D201 resins have excellent mechanical strength, Donnan membrane impact, and stable physicochemical characteristics [14]. In particular, the D201 resin surface has positively charged functional groups conducive to heavy metal adsorption [15]. The ion exchange-surface deposition technique is one of the most widespread techniques for preparing $MnFe_2O_4$/D201 nanocomposites. The mass transfer controlling stage is the diffusion process of ionic components, because ionic components can spread out on the resin surface and the inner surface and react quickly with the functional groups on the resin surface. Thus, if modified with magnetic nanomaterials such as $MnFe_2O_4$, $MnFe_2O_4$/D201 nanocomposites can be used as excellent adsorbents for removing different types of pollutants, including anions from water. Because $MnFe_2O_4$/D201 nanocomposites contain abundant $MnFe_2O_4$ and quaternary ammonium groups, such modified materials are predicted to have a high attraction for As(V) in water.

In this work, $MnFe_2O_4$ was loaded on D201 through a coprecipitation approach for water treatment purposes, which can improve the high selectivity adsorption capacity and deep-treatment ability of materials toward pollutants such as As(V). Various characterization methods, including Fourier transform infrared spectroscopy (FTIR), X-ray diffraction (XRD), thermogravimetric analysis (TGA), scanning electron microscopy (SEM), vibrating sample magnetometry (VSM), Brunauer-Emmett-Teller (BET) surface area, zeta, and X-ray photoelectron spectroscopy (XPS) analyses were used to characterize the composite structure and magnetic and physicochemical properties of the synthesized nanocomposite. Adsorption kinetics and adsorption isotherms were used to explore the adsorption mechanism in the presence of $MnFe_2O_4$/D201. The pH level, contact time, temperature, initial As(V) concentration, coexisting ions, and regeneration were studied through batch experiments. A fixed-bed column experiment with As(V) was conducted to assess its potential for practical applications. The underlying removal mechanisms were analyzed.

2. Materials and Methods

2.1. Materials.
D201 resin was purchased from Tianjin Delite Environmental Protection Technology Co., Ltd. (Tianjin, China). Before use, D201 was treated with 1 M NaOH and 0.1 M HCl solution. Then, D201 is vacuum dried at 50°C for 24 h. $KMnO_4$, $FeSO_4$, NaCl, $NaNO_3$, Na_2SO_4,

and Na_3PO_4 were bought from Sinopharm Chemical Reagent Co., Ltd. (Shanghai, China).

2.2. Preparation of $MnFe_2O_4$/D201.
The $MnFe_2O_4$/D201 was prepared by using a one-pot coprecipitation approach. In a standard synthesis procedure, add a certain quantity of $FeSO_4$ and $KMnO_4$ to 100 mL of deionized water, and stir until resolved. Afterward, 20 g of D201 was accurately added to the system. The solution was adopted by mixing at 298 K for several hours to permit the precursor to disperse inside D201. Then, 3 M NaOH solution was slowly added to the above mixed solution to obtain $MnFe_2O_4$/D201. The obtained $MnFe_2O_4$/D201 were soaked in alkaline environment for 12 h. Filter $MnFe_2O_4$/D201 out of the NaOH solution and clean them with 5 wt% NaCl solution several times until the supernatant arrives at neutral (pH = 7), followed by drying at 298 K to acquire the resulting nanocomposite adsorbents [10].

Adjust the mass ratios for $MnFe_2O_4$ to D201 as $MnFe_2O_4$/D201-5%, $MnFe_2O_4$/D201-10%, $MnFe_2O_4$/D201-15%, $MnFe_2O_4$/D201-20%, and $MnFe_2O_4$/D201-25%; several different adsorbents were prepared. For comparison, bare D021 without $MnFe_2O_4$ as the comparison material of the adsorption experiment. A schematic diagram for the novel preparation process can be obtained in Figure 1.

2.3. Batch Adsorption Experiments.
The primary condition of batch adsorption experiments is to use 0.5 g/L adsorbent, keep the stirring speed at 150 rpm, and control the temperature at 25°C. The influences of pH, reaction time, initial concentration of As(V), and coexisting competing anions on the adsorption process were studied. For the pH in the As(V) solution, diluted HCl and NaOH solution (0.1 mol/L) are used to adjust the solution. The residual contents of As(V) were analyzed through an inductively coupled plasma atomic emission spectroscopy (ICP-AES) instrument [16]. The quantities of As(V) adsorbed onto $MnFe_2O_4$/D201 were estimated by comparing the changes in As(V) concentration before and after. The adsorption capacity was depicted as follows in Text S1.

Varying parameters' impact on the adsorption process was examined, including pH, contact time, initial concentration, and temperature. The effect of pH on As(V) removal was calculated by changing the pH from 3 to 11. For kinetic, explore the adsorption performance under different adsorption times (0-360 min). For adsorption isotherm experiments, it was examined at 298 K, 318 K, and 338 K within the initial As(V) concentration altered from 30 to 100 mg/L. The effects of coexisting ions were examined in 100 mL of 30 mg/L As(V) solutions containing 50 mg $MnFe_2O_4$/D201 and three different dosages (0.01 M, 0.1 M, and 1 M) of NaCl, $NaNO_3$, Na_2SO_4, and Na_3PO_4.

2.4. Recycle Experiment.
The regeneration of $MnFe_2O_4$/D201 was studied by using adsorption-desorption experiments. NaOH solution (0.1 mol/L) was selected as eluent to release As(V) from composite adsorbents. The As(V) adsorbed was wagged with 50 mL of an aqueous NaOH solution for 3 h. Then, $MnFe_2O_4$/D201 was accumulated, washed with
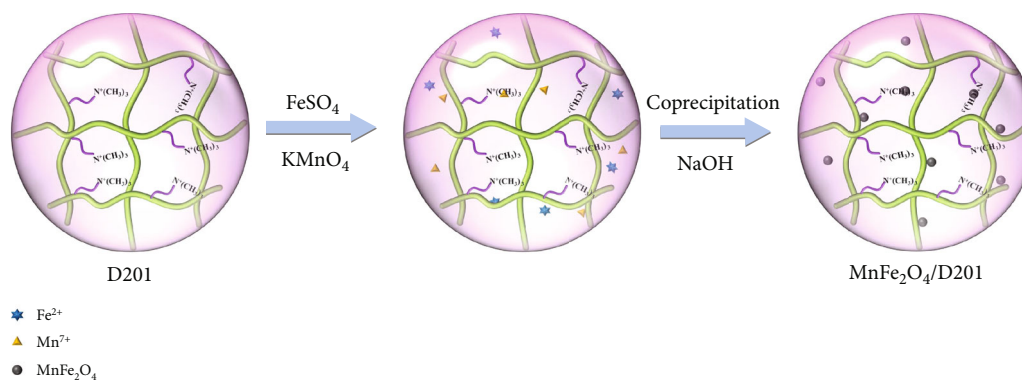
FIGURE 1: The flow chart of MnFe$_2$O$_4$-D201.

deionized water, and dried in a vacuum at 60°C for 12 h. After that, the As(V) removal experiment was restated with the regenerated MnFe$_2$O$_4$/D201. The cycle was repeated 10 times and As(V) removal efficiency was tested each time.

2.5. Fixed-Bed Column Experiments. Fixed-bed experiments were followed through 20 mL of MnFe$_2$O$_4$/D201 inside a 14 mm diameter and 240 mm length of glass columns. Set the experimental conditions, the empty bed contact time (EBCT) is specified as 10 min, and the solution flow rate of simulated wastewater is specified as 2 mL/min. The solution was kept to run with a peristaltic pump, and an automated fraction collector was picked out to collect the effluent samples. The feeding solutions consisted of 1 mg/L As(V), 10 mg/L SO$_4^{2-}$, 100 mg/L Cl$^-$, 10 mg/L PO$_4^{3-}$, and 100 mg/L NO$_3^-$. The adsorption temperature is at 298 K, 318 K, and 338 K.

3. Results and Discussion

3.1. Characterization of Composite Adsorbent MnFe$_2$O$_4$/D201. The FTIR spectra are depicted in Figure 2(a). The FTIR spectra of D021 and MnFe$_2$O$_4$/D201 indicate that they have near typical peaks and patterns, pointing out that the surface functional groups of D201 do not change in structure after the loading of MnFe$_2$O$_4$. For D201 resin, the broad peak at 3413 cm^{-1} is ascribed to -OH bands of H$_2$O. The peaks at 1482 cm^{-1} and 1226 cm^{-1} are credited to -CH and -CN bands, respectively. Further, the peak at 1627 cm^{-1} is ascribed to C=C stretching vibration, showing the existence of D201 resin's styrene frame. The peak at 986 cm^{-1} is ascribed to the feature of the -N$^+$(CH$_3$)$_3$ band, implying the presence of -N(CH$_3$)$_3$ on D201. For MnFe$_2$O$_4$/D201, the raw peaks at 1160 cm^{-1} were the same as metal hydroxyl groups (M-OH, M represented Fe or Mn), which proved that MnFe$_2$O$_4$ was successfully loaded on D201's surface [17, 18].

The XRD diffraction patterns of D021 and MnFe$_2$O$_4$/D201 before adsorption are shown in Figure 2(b). The XRD spectrum of D201 reveals no apparent typical peaks, implying the amorphous nature of D201 resin. The XRD patterns of MnFe$_2$O$_4$/D201 showed a clear characteristic peak of MnFe$_2$O$_4$ at 14.2°, 16.9°, and 25.7°, suggesting that

MnFe$_2$O$_4$ nanocomposite had been successfully located on D201 [19, 20].

The thermal stability of D021 and MnFe$_2$O$_4$/D201 composite was measured by TGA in Figure 2(c). As illustrated in the curve, D021 and MnFe$_2$O$_4$/D201 have three steps in the thermal weight loss process, including bound water loss and composite degradation, and remain breakdown. For MnFe$_2$O$_4$/D201, the weight loss (18%) up to 328°C was probably due to the dehydration process. What is more, the 17% weight loss between 328 and 384°C was attributed to the carbonization of MnFe$_2$O$_4$/D201, and the 27% weight loss in the scope of 384-465°C was attributed to the degradation of MnFe$_2$O$_4$/D201 [21]. Compared with resin D201, the improvement of thermal stability of adsorbent MnFe$_2$O$_4$/D201 with loading of particle MnFe$_2$O$_4$ will help MnFe$_2$O$_4$/D201 to be more suitable for application in the actual environment with higher temperature.

The morphologies of D021 and MnFe$_2$O$_4$/D201 are shown in Figure 3. MnFe$_2$O$_4$/D201 exhibits a ball-shaped formation and has 0.6 mm in average diameter. Here, loaded MnFe$_2$O$_4$ on D201 possesses several advantages. First, the porous morphology can significantly raise the surface accessibility between MnFe$_2$O$_4$/D201 and As(V). Second, D201 can effectively stop MnFe$_2$O$_4$'s agglomeration with excellent stability. When MnFe$_2$O$_4$ is loaded on the resin D201, there are some particles on its surface, and the surface of MnFe$_2$O$_4$/D201 becomes rough [22, 23]. These findings support the successful synthesis of the adsorbent material MnFe$_2$O$_4$/D201. In addition, the mapping of D201 and MnFe$_2$O$_4$/D201 is displayed in Figure 3. For D201, N and O atomic contents are worked out, showing that the N and O are essential elements in D201. For MnFe$_2$O$_4$/D201, N, O, Mn, and Fe contents are calculated to be 5, 29, 14, and 52%, respectively, suggesting that there are MnFe$_2$O$_4$ onto D201, which are contributing to adsorb As(V). From the distribution of different elements in the mapping of MnFe$_2$O$_4$/D201, it can be seen that compared with the existing nanoparticle loading technology, the nanoparticle MnFe$_2$O$_4$ distribution in the adsorbent MnFe$_2$O$_4$/D201 is more uniform, which is conducive to the removal of As(V). The structure of MnFe$_2$O$_4$/D201 likely contributed to more adsorptive sites for As(V) removal.

To confirm that the adsorbent formation existed, N$_2$ adsorption-desorption isotherm characterization was
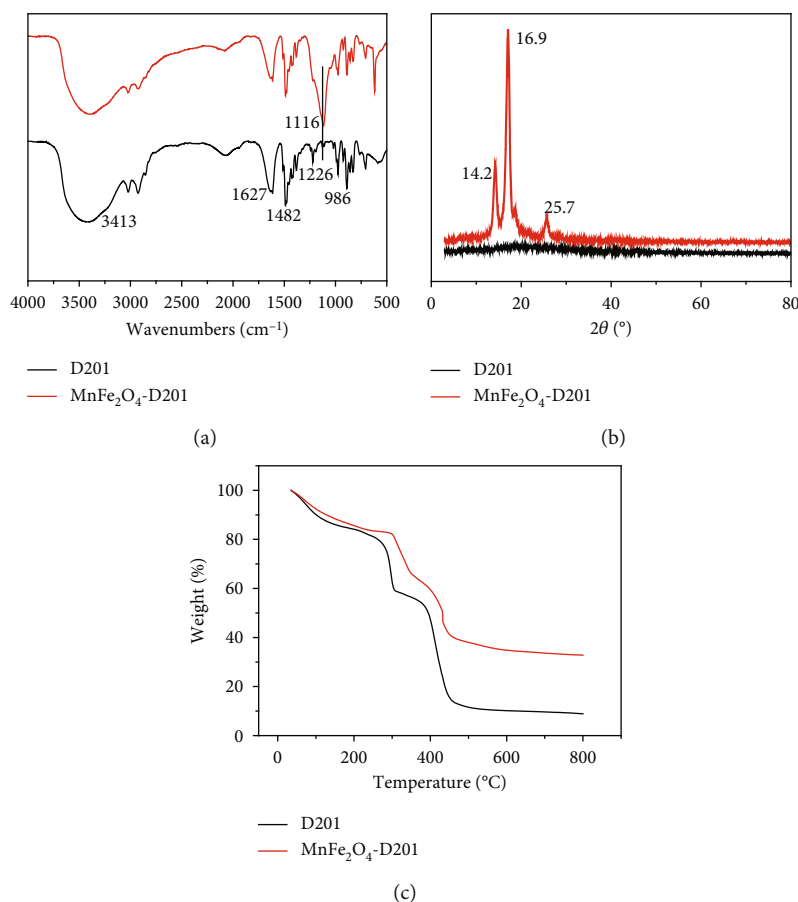
Figure 2: FTIR spectra (a), XRD patterns (b), and TGA (c) of D201 and $MnFe_2O_4$-D201.
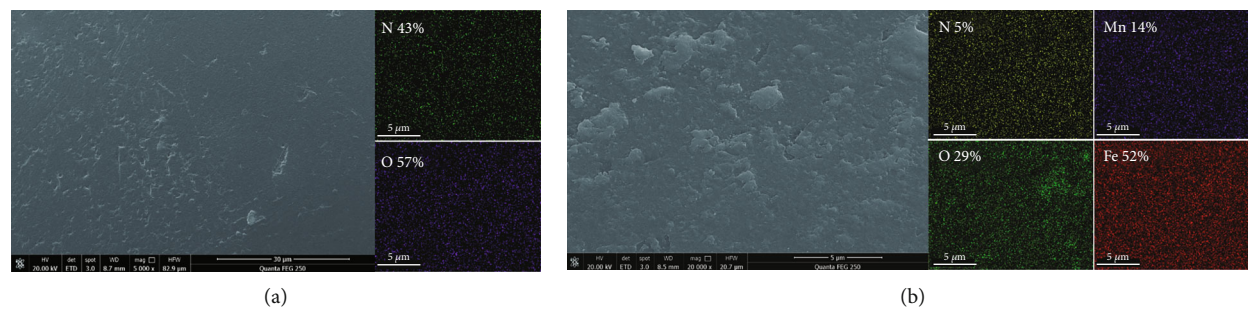

Figure 3: SEM image and mapping of D201 and $MnFe_2O_4$-D201 before adsorption of As(V).

performed. The specific surface area and pore size of $MnFe_2O_4$/D201 were also analyzed using the BET method. As depicted in Figure S1a, $MnFe_2O_4$, D201, and $MnFe_2O_4$/D201 follow a type IV isotherm and have a hysteresis loop at higher relative pressure. $MnFe_2O_4$, D201, and $MnFe_2O_4$/D201 are mesoporous materials. The BET surface areas of $MnFe_2O_4$, D201, and $MnFe_2O_4$/D201 are 9.5, 18.3, and 11.2 m^2/g, respectively [24, 25]. Moreover, the diameters of D201 and $MnFe_2O_4$/D201 with a sharp distribution were approximately 2.8, 11.5, and 3.7 nm, respectively. The surface area, average pore diameter, and pore volume of $MnFe_2O_4$/D201 are less than those of D201, showing the successful functionalization through moieties as nanoparticles attached

to D201 hindered the entry of nitrogen gas into the nanocomposite surface. On the other hand, D201's higher S_{BET} indicated that D201 could effectively prevent the self-agglomeration of $MnFe_2O_4$ nanoparticles. The possible reason is a large number of metal ions (Fe^{2+} and Mn^{7+}) were loaded onto the pore channels of D201 through water at the first stage of the preparation of the adsorbent material $MnFe_2O_4$/D201. D201 with higher S_{BET} has a large number of active sites (-$N^+(CH_3)_3$ groups) uniformly dispersed in the pores. The -$N^+(CH_3)_3$ groups on the resin D201 would promote the diffusion of metal ions when chemical forces occur. After in situ growth preparation process of $MnFe_2O_4$/D201, the nanoparticle $MnFe_2O_4$ was more dispersed on

pore channels of the resin D201 through D201's higher S_{BET}. It may be expected that S_{BET} and pore volume will advance the adsorption capacity of As(V) by providing more active adsorption sites and reducing the mass transfer resistance of As(V).

The magnetic characteristics of $MnFe_2O_4$/D201 were evaluated by using a vibrating sample magnetometer (VSM). Importantly, $MnFe_2O_4$/D201 possessed a saturation magnetization (1.6 emu/g), as demonstrated in Figure S1b. Due to the nonmagnetic D201 mediums in $MnFe_2O_4$/D201, thus $MnFe_2O_4$/D201 has a lower saturation magnetization [26]. Further, the magnetic separation and dispersion of the adsorbents were drawn by a magnet, further pointing out that $MnFe_2O_4$/D201 is well separable. At the same time, the structural properties of resin D201, including the excellent mechanical strength and spherical shape, would also bring convenience to the practical application of composite materials $MnFe_2O_4$/D201. Composite materials $MnFe_2O_4$/D201 would combine their advantages to enhance the separation and recovery of nanocomposite after adsorption.

The survey XPS spectra of D201 and $MnFe_2O_4$/D201 are demonstrated in Figure S2. The survey XPS spectrum revealed the existence of C1s, O1s, N1s, Fe2p, and Mn2p on the sample surface of $MnFe_2O_4$/D201 [27]. However, Fe2p and Mn2p spectra are not apparent in the XPS spectra of $MnFe_2O_4$/D201, probably for the reason that several $MnFe_2O_4$ nanoparticles are imbedded in D201 resin's inner channels.

3.2. Adsorption Study of $MnFe_2O_4$/D201 for As(V) Removal

3.2.1. The Effect of $MnFe_2O_4$ Content on $MnFe_2O_4$/D201 for As(V) Removal. The effect of $MnFe_2O_4$ content on As(V) adsorption capacity of $MnFe_2O_4$/D201 is shown in Figure S3. Although the resin itself has a large specific surface area and a certain amount of effective functional groups, its adsorption capacity for As(V) still has certain limitations. Compared with many reported adsorption materials, the adsorption performance of D201 is not outstanding. With the addition of nanoparticles $MnFe_2O_4$, its adsorption performance has significantly improved. $MnFe_2O_4$/D201-15% has the most effective removal on As(V), and the adsorption capacity arrives at 35.8 mg/g. On the one hand, $MnFe_2O_4$ was developed by $MnFe_2O_4$/D201 which has the potential to adsorb As(V). On the other hand, the styrene frame of D201 can distribute $MnFe_2O_4$, and the resin surface accommodates a massive quantity of $-N^+(CH_3)_3$ groups. The As(V) adsorption capacities declined in the presence of $MnFe_2O_4$/D201-20% and $MnFe_2O_4$/D201-25%, which was attributed to $MnFe_2O_4$ nanoparticle aggregation on the D201. Therefore, $MnFe_2O_4$/D201-15% was selected for further experiments.

3.2.2. The pH_{pzc} of $MnFe_2O_4$/D201 and the Influence of pH on As(V) Removal. The pH action is a critical factor because of its double effect on the ionic form of the adsorbate and the surface charge of the adsorbent. To probe the effect of pH and achieve excellent As(V) adsorption, the zeta potential

analysis of adsorbents and adsorption experiments at varying pH levels were conducted. According to the references, the nanoparticle $MnFe_2O_4$ has a low pH_{pzc} value, so $MnFe_2O_4$ presents negative charge in a wide range of pH. $MnFe_2O_4$ has a repulsive effect with As(V), which results in poor adsorption capacity. There are a large number of $-N^+(CH_3)_3$ groups on the resin D201, which can improve the electrical properties of the composite within the whole pH range and increase the material's pH_{pzc} value. For $MnFe_2O_4$/D201, as acidity increases, the charge of the adsorbent particles tends to be positive, as shown in Figure 4(a). Both D201 and the impregnated $MnFe_2O_4$ are positively charged and adsorb anions by electrostatic attraction [28].

Meanwhile, for $MnFe_2O_4$/D201, the composite adsorbent's removal efficiency gradually declines as pH increases, as shown in Figure 4(b). For As(V), $H_2AsO_4^-$ is the dominate species at pH 2-7, whereas the dominant As ion formed is $HAsO_4^{2-}$ as pH increases, as shown in Figure 4(c). When pH < 7, $MnFe_2O_4$/D201 with positively charged would adsorb more $H_2AsO_4^-$ by electrostatic attraction [29]. With an increase in pH, a large amount of OH^- would lead to competitive adsorption with As(V) on $MnFe_2O_4$/D201, resulting in insufficient adsorption capacity. Notably, the adsorption capacity is 26.3 mg/g at pH 8. The removal efficiency slightly declines in the pH range of 3-7, whereas it declines sharply in the range of 8-11. A highly acidic water environment would lead to the risk of posttreatment. Thus, the best pH for As(V) adsorption was 7, which is the optimum pH of adsorption. These finding confirmed that pH has a critical effect on As(V) adsorption. $MnFe_2O_4$/D201 exhibited a positive charge at pH 3-8 and promoted the adsorption of negatively charged As(V) by electrostatic attraction.

3.2.3. Adsorption Kinetic Analysis. Contact time was also a critical factor in the As(V) adsorption process. Kinetic experiments demonstrated that $MnFe_2O_4$/D201 could quickly reach adsorption equilibrium by supplying $-N^+(CH_3)_3$ groups and $MnFe_2O_4$ (Figures 5(a) and 5(b)). As is visible, all kinetic adsorption curves could be around segmented into two consecutive adsorption steps; the As(V) adsorption capacities by the $MnFe_2O_4$/D201 were sharply raised throughout the first 60 min and the adsorption capacity would not increase after 240 min. While contact time was passed 240 min, adsorption capacity's raises were nearly insignificant, indicating that 240 min could be considered with the adsorption equilibrium time. The maximum equilibrium adsorption capacities (q_e) are 38 and 38.9 mg/g for As(V), respectively. The rapid adsorption of As(V) may be associated with a lot of directly uncovered active adsorption sites and the porous structure of the $MnFe_2O_4$/D201 [30], which was contributed to the adsorption and diffusion of As(V). After that, unsaturated adsorption sites were filled, and the growth rate of adsorption began to went down [31].

To better investigate and interpret the adsorption behavior, pseudo-first-order [32], pseudo-second-order [33], and Elovich models [34] (Text S1) were analyzed. The parameters derived from adsorption kinetic curves are listed in
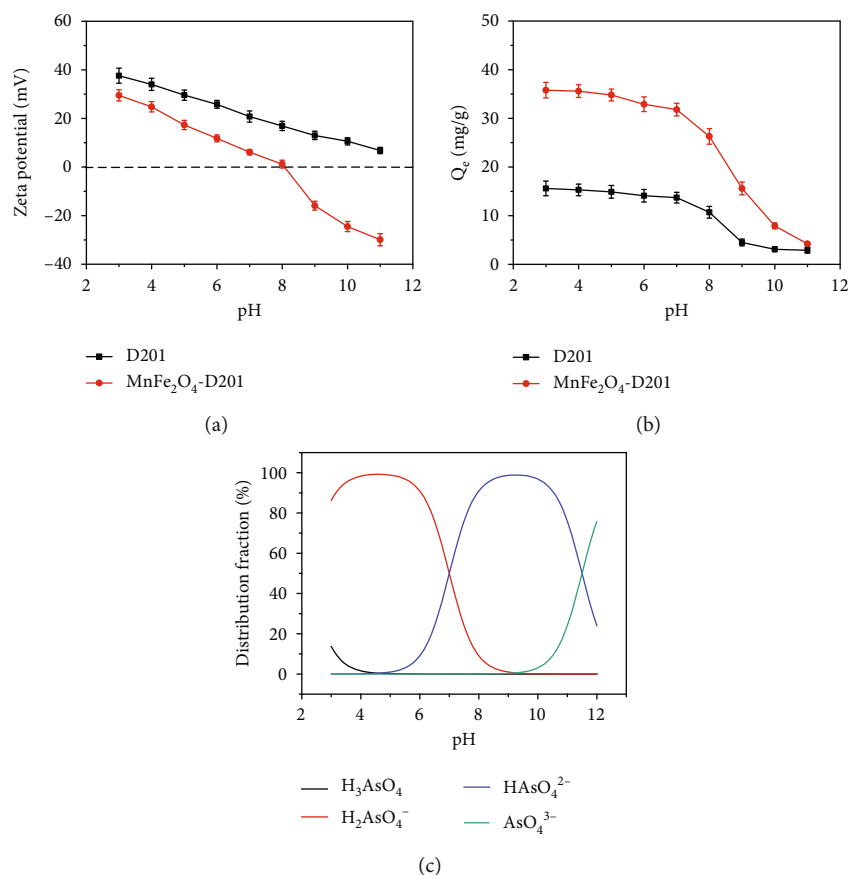
(a)

(b)

(c)

FIGURE 4: Zeta of D201 and MnFe$_2$O$_4$-D201 (a). Effects of pH value on the uptake of As(V) adsorption by D201 and MnFe$_2$O$_4$-D201 (b). Fraction of As(V) species at different pH (c) (the uniform experimental condition: 100 mL of 30 mg/L As(V) with 50 mg D201 or MnFe$_2$O$_4$/D201, 150 rpm, 25°C, and 360 min).

Table 1. The fitting data in Table 1 indicate that the pseudo-second-order model describes the sorption kinetics better than the pseudo-first-order and Elovich models. The adsorption mechanism corresponding to the pseudo-second-order kinetic is that the control factor of adsorption is chemical interaction, which occurred via electrostatic attraction or complexation between adsorbent and As(V) [35]. The k_2 values of As(V) on D201 and MnFe$_2$O$_4$/D201 were 0.0004 and 0.0008 g/(mg*min) (Table 1), respectively. This indicated that MnFe$_2$O$_4$/D201 had the highest adsorption rate and quickly promoted As(V) removal from aqueous solution. The reason may be that MnFe$_2$O$_4$ on the surface of the MnFe$_2$O$_4$/D201 is conducive to the adsorption of As(V). The fit of the data to the pseudo-first-order and Elovich models also matches well. The data overall suggest that the rate-limiting kinetic process for the removal of As(V) from solution was mainly the electrostatic attraction and complexation, with a certain degree of diffusion on highly heterogeneous surface of the adsorbent. In a word, the adsorption process may include the following steps: the As(V) migrated from the liquid phase to the outer surface of the MnFe$_2$O$_4$/D201, continued to migrate on the surface until enter the pores of MnFe$_2$O$_4$/D201, and loaded to the active site of the MnFe$_2$O$_4$/D201 through this process until the adsorption reaches saturation.

3.2.4. Adsorption Isotherm Analysis. The effect of initial As(V) concentration on As(V) adsorption over the surface of MnFe$_2$O$_4$/D201 was studied as shown in Figures 5(d)–5(f). When the As(V) initial concentration was increased from 30 to 100 mg/L at 298 K, the As(V) adsorption capacity was expanded from 35.8 mg/g to 41 mg/g. That is because the adsorption process enhances in the mass transfer driving force [36]. Then, the adsorption capacity of MnFe$_2$O$_4$/D201 has not significantly changed as the As(V) concentration increases again, because the active sites of MnFe$_2$O$_4$/D201 are saturated.

To better understand the interaction mechanisms between As(V) and MnFe$_2$O$_4$/D201, the isotherm models of Langmuir [37], Freundlich [38], and Temkin [39] (Text S1) were evaluated (Figures 5(c) and 5(d)). The suitability of isotherm fit of experimental data was evaluated using nonlinear chi-square test (χ^2) [40] and hybrid fractional error function [41], which are calculated using the following at Text S1. The relation between temperature and equilibrium concentration was examined at varying temperatures (298, 318, and 338 K). The Langmuir model supposed monolayer sorption's structure onto a concrete surface with similar and energetically equivalent active sites, whereas the Freundlich isotherm model thought multilayer sorption's network onto a heterogeneous surface. These models' linear
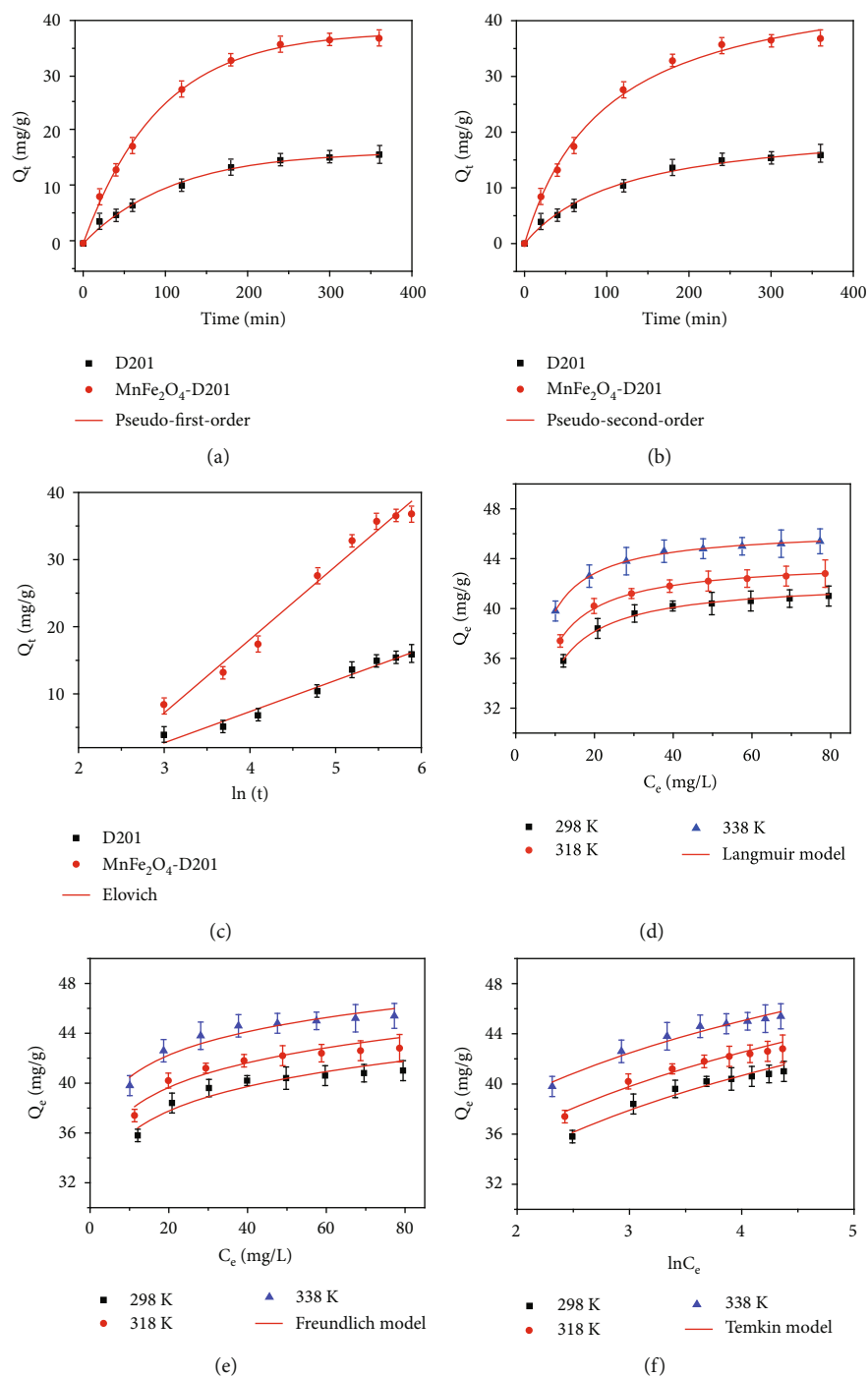
FIGURE 5: Adsorption kinetics of As(V) at 298 K (a–c). Adsorption isotherm of As(V) at 298 K, 318 K, and 338 K (d–f) (the uniform experimental condition: 100 mL of As(V) with 50 mg D201 or $MnFe_2O_4$/D201, 150 rpm; adsorption kinetics: adsorption times are 0-360 min and 30 mg/L As(V); adsorption isotherm: temperature at 298 K, 318 K, and 338 K, As(V) concentration range is 30 to 100 mg/L).

TABLE 1: As(V) adsorption kinetic model constants derived from the pseudo-first-order, the pseudo-second-order equation, and the Elovich model.

Adsorbents	The pseudo-first-order			The pseudo-second-order			Elovich		
	k_1 (min^{-1})	q_e (mg/g)	R^2	k_2 (g/(mg·min))	q_e (mg/g)	R^2	α (mg/g*min)	β (mg/g)	R^2
D201	0.009	16.5	0.987	0.0004	21.7	0.992	4.67	0.215	0.969
$MnFe_2O_4$-D201	0.011	38.0	0.984	0.0008	38.9	0.994	10.88	0.092	0.979

TABLE 2: Adsorption isotherm model constants for the adsorption of As(V).

T (K)	Langmuir model					Freundlich model					Temkin model				
	K_L (L/mg)	q_{max} (mg/g)	Hybrid fraction	R^2	χ^2	K_F (mg$^{1-n} \cdot$L$^n \cdot$g^{-1})	n	Hybrid fraction	R^2	χ^2	B	K_T (L/mg)	Hybrid fraction	R^2	χ^2
298	0.467	42.2	0.075	0.994	0.004	30.34	13.68	0.170	0.898	0.060	257.7	17.19	57.45	0.954	67.65
318	0.519	43.9	0.019	0.997	0.002	32.15	14.28	0.409	0.900	0.056	279.4	22.35	53.89	0.960	63.66
338	0.602	46.4	0.011	0.998	0.001	35.01	15.95	0.045	0.920	0.049	315.6	39.28	46.87	0.969	53.75

TABLE 3: Thermodynamic parameters for the adsorption.

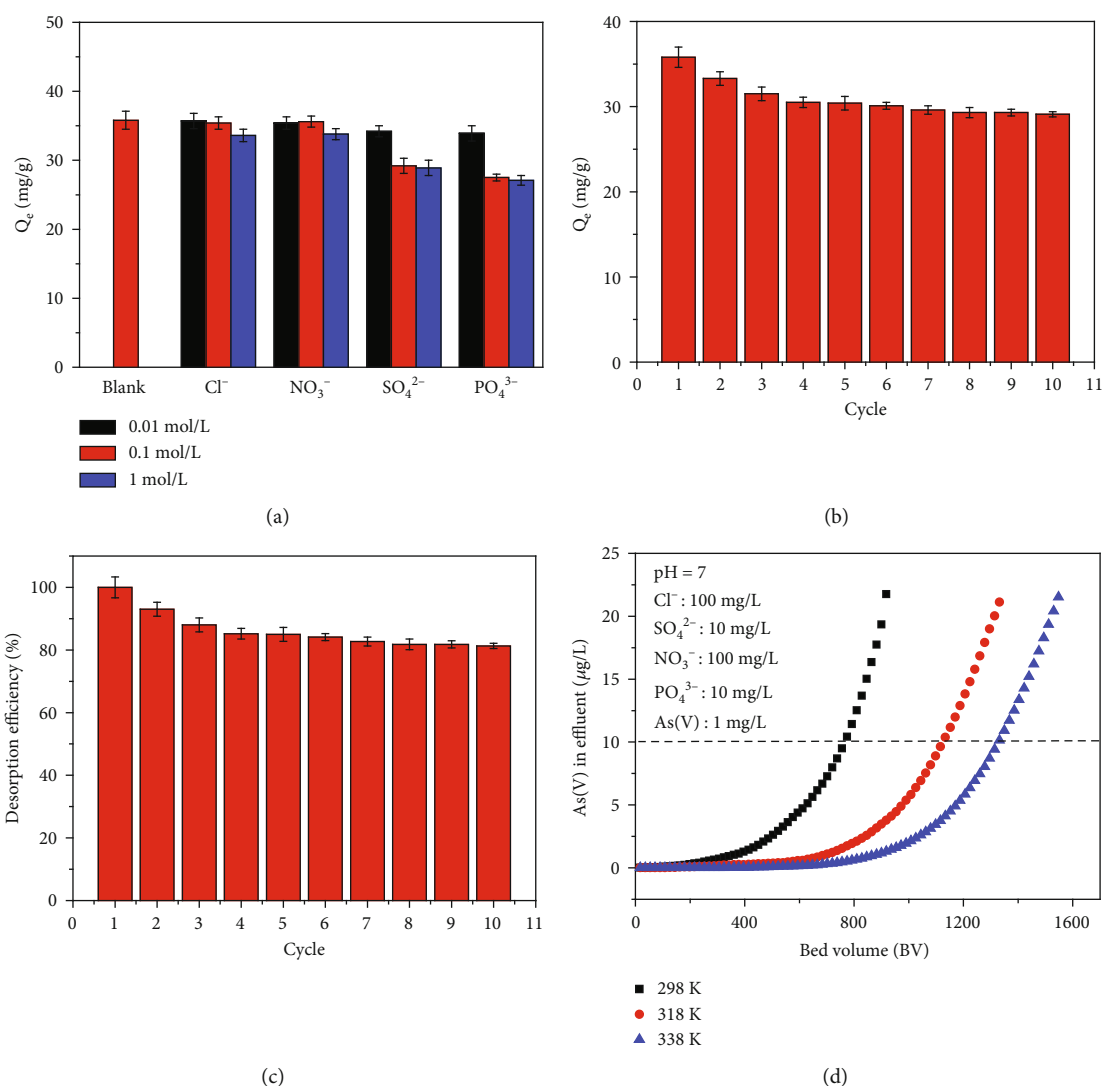| Adsorbent	Temperature (K)	ΔG (kJ/mol)	ΔH (kJ/mol)	ΔS (kJ/(mol*K))
	298	-38.13		
$MnFe_2O_4$-D201	318	-40.96	5.34	0.15
	338	-43.96		

(a)

(b)

(c)

(d)

FIGURE 6: Effects of coexistent ions and ionic strength on As(V) adsorption (a). Adsorption-desorption experiments of As(V) for $MnFe_2O_4$-D201 on adsorption capacity (b) and desorption efficiency (c). Fixed-bed column experiment with simulated wastewater effluent (d) (the uniform experimental condition: 100 mL of 30 mg/L As(V) with 50 mg $MnFe_2O_4$/D201, 150 rpm, 25°C, and 360 min; (a) salt ion concentration on 0.01 M, 0.1 M, and 1 M; (b, c) 50 mL of 0.1 mol/L NaOH solution for 3 h; (d) the solution flow rate at 2 mL/min, 1 mg/L As(V), 10 mg/L SO_4^{2-}, 100 mg/L Cl^-, 10 mg/L PO_4^{3-}, and 100 mg/L NO_3^-, at 298 K, 318 K, and 338 K).

forms are offered by the equations according to Text S1. Langmuir, Freundlich, and Temkin isotherm models' fitting parameters on As(V) adsorption are listed in Table 2. The higher R^2 on the Langmuir model (0.995) implies that As(V) adsorption process can be better depicted by the Langmuir model. Moreover, the adsorption capacity calculated by the Langmuir equation was closer to the experimental results. The low values of Pearson's chi-square measured

error (χ^2) and hybrid fractional error suggest that the Langmuir well explained the As(V) uptake isotherm on to $MnFe_2O_4$/D201 among the three models tested. Langmuir's isotherm indicates adsorbates' homogeneous adsorption on vigorous equivalent sites [42]. Therefore, the adsorption of As(V) ions took place as a monolayer on $MnFe_2O_4$/D201 nanocomposites [43]. When the temperature is 298, 318, and 328 K, the expected maximal capacities of $MnFe_2O_4$/

D201 were taken from the Langmuir model, and the value is 42.2, 43.9, and 46.4 mg/g, showing that the rise of temperature promotes the progress of adsorption process. Moreover, $1/n$ (298-338 K) are all under 1, pointing out that $MnFe_2O_4/$ D201 can adsorb As(V) spontaneously [44]. The values of R_L ($0 < R_L < 1$) for the adsorption of As(V) ions lie between 0.467 and 0.602, indicating the suitability of the sorption process and the excellent affinity between the As(V) and the $MnFe_2O_4/D201$ composite adsorbent. As a result, the adsorption process was single-layer adsorption, suggesting that the $MnFe_2O_4/D201$ surface was homogeneously distributed adsorption active sites [45].

3.2.5. Adsorption Thermodynamics. Adsorption thermodynamic characteristics were examined at 298-338 K to determine the effect of temperature on As(V) removal capacity. Three thermodynamic parameters, including Gibbs free energy, entropy, and enthalpy, are presented in Table 3 and Figure S4. The entropy and enthalpy were calculated from the incline and intercept of the adsorption data fitted adopting equation (Text S1). The Gibbs free energy as negative values for the As(V) uptake reactions by $MnFe_2O_4/D201$ indicates spontaneity of the adsorption process (Table 3). As the temperature rose, it was also noticed that the Gibbs free energy value rose, implying a greater driving force and thus a higher adsorption affinity at higher temperatures. The high positive values of enthalpy (5.34 kJ/mol) indicate that As(V) adsorption process over the $MnFe_2O_4/D201$ is endothermic and the adsorption process is involved in chemical interactions [40, 46]. The presence of a positive entropy values (0.15 kJ/ (mol*K)) indicates that As(V) variability rises during process and the $MnFe_2O_4/D201$ has a significant affinity for As(V) [41, 47].

3.2.6. Effect of Coexisting Competing Anions towards As(V) Adsorption. The ionic strength of the solution and adsorption performance would be affected by coexisting anions. Selective adsorption of As(V) with anions (Cl^-, NO_3^-, SO_4^{2-}, and PO_4^{3-}) was investigated for $MnFe_2O_4/D201$. For coexisting anions, multivalent anions (SO_4^{2-}, PO_4^{3-}) possess a more substantial affinity for $MnFe_2O_4/D201$ than monovalent anions (Cl^-, NO_3^-) in Figure 6(a). The effect of Cl^- and NO_3^- (0.01-0.1 mol/L) on the adsorption capacity of As(V) by using $MnFe_2O_4/D201$ is nearly unchanged. Only when the concentration of Cl^- and NO_3^- increases to 1 mol/L, the adsorption capacity would decrease slightly. Compared with Cl^- and NO_3^-, the addition of SO_4^{2-} and PO_4^{3-} leads to an apparent drop in adsorption capacity, but further raising the concentration of the competing anions results in an unvarying q_e value at 27.5 mg/g [48]. The As(V) adsorption of $MnFe_2O_4/D201$ reduced in the following order: $PO_4^{3-} > SO_4^{2-} > NO_3^- > Cl^-$. A potential reason is that both SO_4^{2-} and PO_4^{3-} have more charges, which easily make them inhibit the electrostatic attraction between the D201 host and As(V) [49]. At the same time, the inner sphere complex structure between As(V) and $MnFe_2O_4$ was unaffected [50]. The adsorption sites on D201 would be affected by the competition between the As(V) and the coexisting anions,
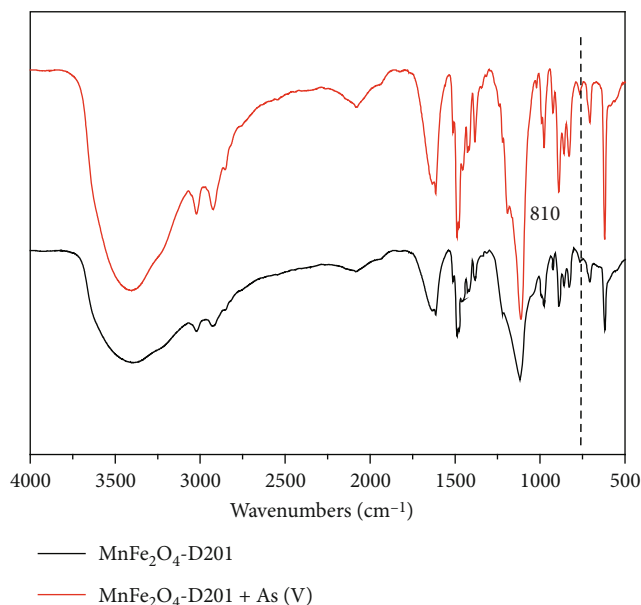

FIGURE 7: FTIR of $MnFe_2O_4$-D201 before and after adsorption of As(V).

thereby having a slight impact on the adsorption capacity of $MnFe_2O_4/D201$.

It shows that $MnFe_2O_4$ modification enhanced the selective adsorption on $MnFe_2O_4/D201$. D201 can just capture As(V) through the structure of an outer sphere complex or nonspecific electrostatic attraction. In contrast, the immobilized $MnFe_2O_4$ nanoparticles could separate As(V) following ligand exchange or a specific Lewis acid-base interaction. This study's consequences demonstrated that $MnFe_2O_4/$ D201 is efficient and selective in removing possibly hazardous As(V) from complex polluted industrial effluents and groundwaters.

3.2.7. Desorption and Reusability Study. In general, the recyclability of adsorbents can enhance the economics of the remediation process. To investigate the recyclability and reusability of adsorbents, the adsorption capacity of $MnFe_2O_4/D201$ was explored for ten cycles. The adsorption capacity is 33.3 mg/g for two reusing runs, higher than 30.4 mg/g for five reusing runs, and higher than 29.1 mg/g for the ten reusing runs (Figure 6(b)). For the adsorbent $MnFe_2O_4/D201$, in addition to keeping the adsorption capacity at a high level, its other advantage over $MnFe_2O_4$ is that the material quality of $MnFe_2O_4/D201$ is basically unchanged. In the field of adsorption, most powdered adsorbents have limitations, including the quality loss of adsorbents and the difficult operation on recovery in practical application. Desorption efficiency of adsorbent $MnFe_2O_4/$ D201 is shown in Figure 6(c). $MnFe_2O_4/D201$ presented a good desorption efficiency over 81.3% after ten times of adsorption-desorption cycle. The small drop in the removal efficiencies of As(V) ions over $MnFe_2O_4/D201$ nanocomposite was attributed to the damaged adsorption sites after each cycle [51]. This conclusion is consistent with SEM results of $MnFe_2O_4/D201$ before and after adsorption-desorption
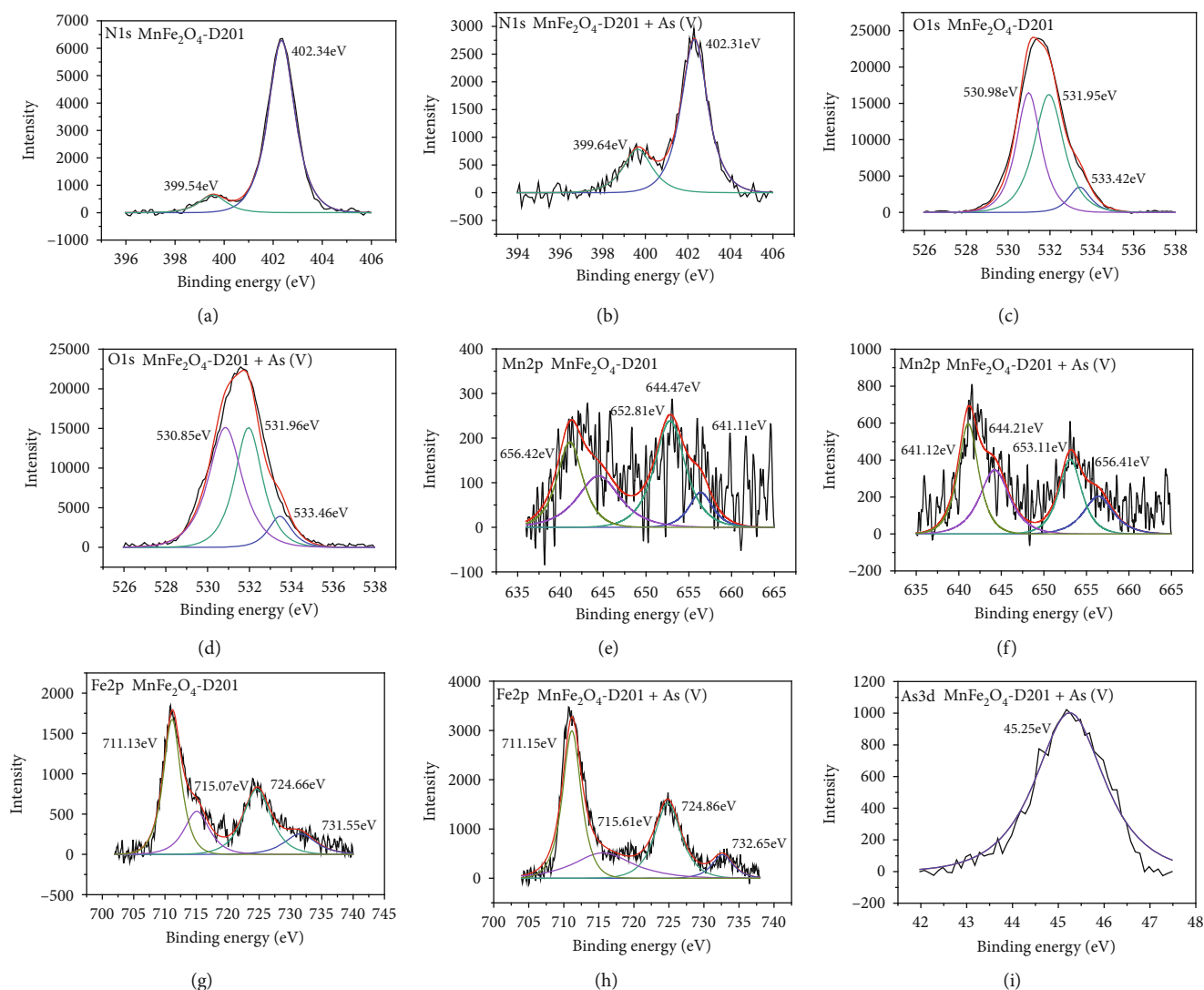
FIGURE 8: N1s (a, b), O1s (c, d), Mn2p (e, f), Fe2p (g, h), and As3d (i) XPS spectra of MnFe$_2$O$_4$-D201 before and after adsorption of As(V).

cycle. As shown in Figure 3, the surface of the adsorbent MnFe$_2$O$_4$/D201 is relatively rough before adsorption. According to the mapping results, the relative percentage contents of N, Mn, and Fe elements at this time are 5%, 14%, and 52%, respectively. After adsorption-desorption cycle, the surface of the adsorbent MnFe$_2$O$_4$/D201 becomes smoother, and the relative percentage content of N, Mn, and Fe elements has slightly decreased in Figure S5. The smooth surface may be caused by the shedding of loaded nanoparticles MnFe$_2$O$_4$ during the desorption process. The relative percentage contents of N, Mn, and Fe elements are 3%, 11%, and 42%, respectively. The active site of the adsorbent mainly contains N, Mn, and Fe elements. It is obvious that the active site of the adsorbent MnFe$_2$O$_4$/D201 is destroyed by the desorption agent during the desorption process, and the content of the active groups has slightly decreased. The controlled drops in sorption-desorption performances indicate the excellent stability and high recyclability of MnFe$_2$O$_4$/D201.

3.2.8. *Fixed-Bed Adsorption.* To further explore MnFe$_2$O$_4$/D201 applied in wastewater, fixed-bed adsorption toward As(V)-contaminated water was studied according to MnFe$_2$O$_4$/D201 into the separated fixed-bed columns. As described in Figure 6(d), the bed volume of MnFe$_2$O$_4$/D201 was about 774 BV (298 K), 1134 BV (318 K), and 1332 BV (338 K) as reported by the breakthrough curves (breakthrough level was 10 μg/L) [52], implying that MnFe$_2$O$_4$/D201 has good As(V) adsorption capacity in wastewater. Also, it was shown that MnFe$_2$O$_4$/D201 possessed the potential for As(V) species removal in water.

3.3. *Adsorption Mechanism of MnFe$_2$O$_4$/D201.* The FTIR analyses were applied to confirm chemical changes during the adsorption process. After adsorbing As(V), a raw peak corresponding with the As-O stretching vibration came out approximately 810 cm^{-1} in Figure 7. This suggested that As(V) was adsorbed onto MnFe$_2$O$_4$/D201 and composed the chemical bond. What is more, the relative intensity of

TABLE 4: Normalized peak areas of XPS spectra in Figure 8.

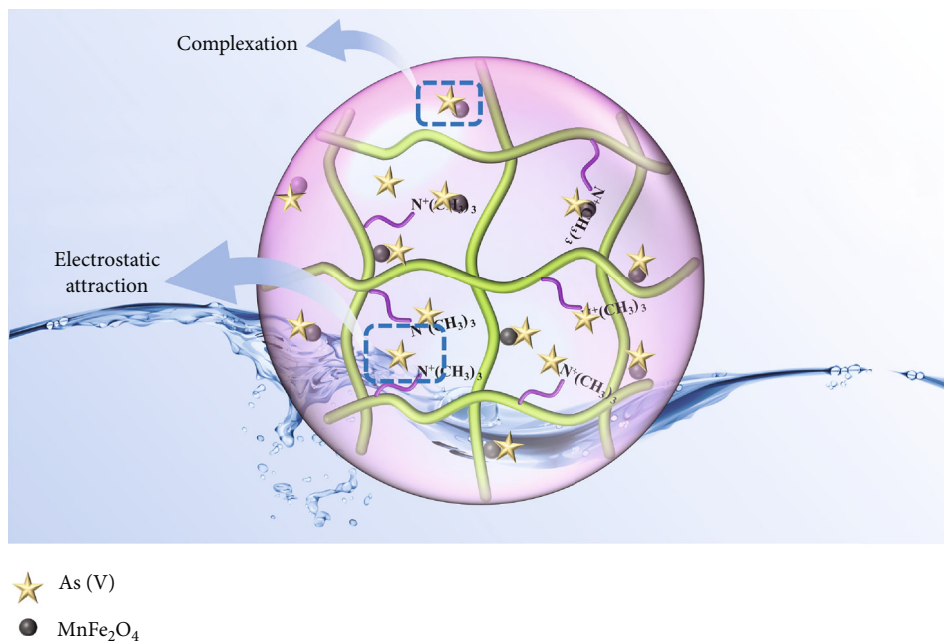| Elements	O1s			N1s	
Elemental species	H_2O	-OH	O^{2-}	$-N^+(CH_3)_3$	-NH-
Locations of peaks	533.42-533.46	531.95-531.95	530.85-530.98	402.31-402.34	399.54-399.64
MnFe$_2$O$_4$-D201	7.81	50.00	42.19	90.47	9.53
MnFe$_2$O$_4$-D201+As(V)	8.82	41.18	50.00	76.19	23.81

☆ As (V)

● MnFe$_2$O$_4$

FIGURE 9: The schematic diagram of adsorption mechanism.

-OH functional groups was decreased after adsorption of As(V), suggesting that the surface complexation between -OH functional groups and As(V) substantially contributed a lot to the adsorption process.

The SEM and mapping of MnFe$_2$O$_4$/D201 after the adsorption process are exhibited in Figure S6. Compared with MnFe$_2$O$_4$/D201, the surface of MnFe$_2$O$_4$/D201 has no apparent changes. And As elements appear on the surface of MnFe$_2$O$_4$/D201 about 3% after adsorption, with decreased Mn and Fe element contents. This result indirectly proves that metal atoms Mn and Fe play a significant part in the adsorption of As(V).

To further realize the adsorption mechanism, XPS spectra were used to probe the chemical state on the surface of the MnFe$_2$O$_4$/D201 composites before and after adsorption, as shown in Figure 8. The high-resolution spectra of N1s of MnFe$_2$O$_4$/D201 are illustrated in Figures 8(a) and 8(b). The characteristic peaks at 402.34 and 399.54 eV belong to $-N^+(CH_3)_3$ and -NH, respectively. After contact with As(V), $-N^+(CH_3)_3$ content is reduced from 90.47% to 76.19%, as shown in Table 4, which is ascribed to the electrostatic attraction between As(V) anions and D201 resin [53, 54]. Figures 8(c) and 8(d) illustrate the O1s XPS spectra of MnFe$_2$O$_4$/D201 before or after adsorbing As(V). The figures show multiple peaks centered at 533.42.2, 531.95, and 530.98 eV, assigned to adsorbed crystal water (H-O-H), the

hydroxyl group bound to metal (M-OH), and the oxide-oxygen (O^{2-}), respectively. After absorbing As(V), the peak area proportion of O^{2-} increased significantly from 42.19% to 50.00%, whereas that of OH$^-$ declined from 50.00% to 41.18%. The results further confirmed that more -OH on the MnFe$_2$O$_4$/D201 surface reacted with As(V). The number of -OH decreased after the reaction, and the inner sphere complexes were formed by complexation between -OH and As(V), which was more steady than the outer sphere complexes formed by electrostatic. To further analyze the role of MnFe$_2$O$_4$, the high-resolution XPS spectra of Mn2p and Fe2p were observed (Figures 8(e)–8(h)). As shown in Figures 8(e) and 8(f), the Mn2p peaks exhibited major peaks before adsorption at 656.42, 652.81, 644.47, and 641.11 eV. The Fe2p peaks exhibited major peaks before adsorption at 711.13, 715.07, 724.66, and 731.55 eV. The binding energies of Mn2p and Fe2p shifted after As(V) adsorption, indicating that Mn and Fe species reacted with As(V) [55, 56]. After adsorption, a raw peak at 45.25 eV is observed in Figure 8(i), attributed to the As^V-O. The As3d's peak indicates that the MnFe$_2$O$_4$/D201 surface adsorbs a significant amount of As(V) during the adsorption process.

Concentrating on the experimental data under varying pH, the adsorption capacity of MnFe$_2$O$_4$/D201 decreases with the increase in pH. The physical electrostatic repulsion enhanced due to the deprotonation of sorbents accompanied

by the increase of pH value. It is speculated that $MnFe_2O_4/$D201 adsorbed As(V) by $-N^+(CH_3)_3$ and $MnFe_2O_4$. Afterward, they supplied electrostatic attraction to negatively charged $H_2AsO_4^-$ or $HAsO_4^{2-}$ and bound it to the material's surface in the form of ionic bonds.

These above consequences confirmed that the adsorption mechanism was electrostatic attraction and complexation. The results were also consistent with the isotherm and kinetic study. Besides, the schema of As(V) removal mechanisms by $MnFe_2O_4/$D201 is illustrated in Figure 9. First, D201 would increase the zeta potential of $MnFe_2O_4/$D201, which is more favorable for electrostatic attraction with As(V). Second, $MnFe_2O_4$ modified the surface structure of $MnFe_2O_4/$D201 and provided more functional groups such as -OH, contributing to complexation with As(V).

4. Conclusion

In this study, the successful combination of the two components ($MnFe_2O_4$ and D201) of the nanocomposite $MnFe_2O_4/$D201 was confirmed by various characterization techniques. Different parameters such as pH, contact time, and initial concentration were examined to define the optimum adsorption conditions. The adsorption of As(V) is affected by the pH value, with As(V) adsorption being the most effective at pH 3. The kinetics and adsorption isotherms of $MnFe_2O_4/$D201 for As(V) followed the Langmuir isotherm model and pseudo-second-order kinetic model, respectively. The adsorption behavior is controlled by chemical adsorption. The maximal adsorption capacity of $MnFe_2O_4/$D201 was 35.8 mg/g, and it attained equilibrium within 240 min. Thermodynamic results showed that the adsorption process was endothermic and spontaneous. The magnetic separation of $MnFe_2O_4/$D201 enhanced its reusability for As(V) removal up to ten successive cycles. Finally, the superior performance in the fixed-bed column experiments confirmed the potential use of $MnFe_2O_4/$D201 as an excellent adsorbent. The efficient As(V) removal by $MnFe_2O_4/$D201 is based on the combined electrostatic attraction and complexation. In summary, because of its facile fabrication process, excellent selectivity adsorption capacity, and deep treatment for As(V) removal, $MnFe_2O_4/$D201 has promising application capability for As(V) sequestration from polluted water.

Data Availability

The data used to support the findings of this study are included within the supplementary information file(s).

Conflicts of Interest

The authors declare that they have no known competing financial interests or personal relationships that could have appeared to influence the work reported in this paper.

Authors' Contributions

Shaopeng Zhang contributed to the conceptualization, methodology, software, investigation, formal analysis, writing of the original draft, and funding acquisition. Jie Ding contributed to the formal analysis and writing of the original draft. Dayong Tian was responsible for the resources and funding acquisition. Feifei Liu was responsible for the investigation and formal analysis. Qiaoling Li investigated the study and wrote the original draft. Minghua Lu contributed to the resources, supervision, and funding acquisition.

Acknowledgments

Supplementary Materials

Supplementary data for this article includes one text (model calculation formulas involved in tables) and six figures, which can be found online after publication. (*Supplementary Materials*)

References

[1] N. S. Alsaiari, F. M. Alzahrani, K. M. Katubi, A. Amari, F. B. Rebah, and M. A. Tahoon, "Polyethylenimine-modified magnetic chitosan for the uptake of arsenic from water," *Applied Sciences*, vol. 11, no. 12, p. 5630, 2021.

[2] E. Bahmani, S. Koushkbaghi, M. Darabi, A. Zabihisahebi, A. Askari, and M. Irani, "Fabrication of novel chitosan-g-PNVCL/ZIF-8 composite nanofobers for adsorption of Cr(VI), As(V) and phenol in a single and temary systems," *Carbohydrate Polymers*, vol. 224, article 115148, 2019.

[3] S. R. Cao, T. T. Tang, C. X. Xi, and Z. Q. Chen, "Fabricating magnetic GO/ZIF-8 nanocomposite for amphetamine adsorption from water: capability and mechanism," *Chemical Engineering Journal*, vol. 422, article 130096, 2021.

[4] T. Chen, Y. F. Wei, W. J. Yang, and C. B. Liu, "Highly efficient As(III) removal in water using millimeter-sized porous granular MgO-biochar with high adsorption capacity," *Journal of Hazardous Materials*, vol. 416, article 125822, 2021.

[5] S. A. Cheng, P. F. Xie, Z. Yu, R. N. Gu, and Y. Q. Su, "Enhanced adsorption performance of UiO-66 via modification with functional groups and integration into hydrogels," *Environmental Research*, vol. 212, article 113354, 2022.

[6] Z. N. Deng, Z. Y. Fang, A. R. Liu, N. Xu, and X. L. Zhang, "From laboratory to large-scale manufacture of anion exchange resin-supported nano-hydrated zirconium oxide for As(V) removal from water solutions," *Science of the Total Environment*, vol. 777, article 146103, 2021.

[7] J. J. Hou, R. Y. Weng, W. W. Jiang et al., "In-situ preparation of novel sedimentary rock-like Fe_3O_4 by rice-husk mesoporous silica as templates for effective remove As(III) from aqueous solutions," *Journal of Environmental Chemical Engineering*, vol. 9, no. 5, article 105866, 2021.

[8] M. B. Jumah, M. H. Eid, A. A. Huqail et al., "Enhanced remediation of As (V) and Hg (II) ions from aqueous environments using β-cyclodextrin/MCM-48 composite: batch and column studies," *Journal of Water Process Engineering*, vol. 42, article 102118, 2021.

[9] Z. H. Khan, M. L. Gao, J. J. Wu, R. Bi, C. T. Mehmood, and Z. G. Song, "Mechanism of As(III) removal properties of biochar-supported molybdenum-disulfide/iron-oxide system," *Environmental Pollution*, vol. 287, article 117600, 2021.

[10] A. Kumar, T. Bhattacharya, W. A. Shaikh, S. Chakraborty, G. Owens, and M. Naushad, "Valorization of fruit waste-based biochar for arsenic removal in soils," *Environmental Research*, vol. 213, article 113710, 2021.

[11] M. Li, B. G. Zhang, S. Q. Zou, Q. S. Liu, and M. Yang, "Highly selective adsorption of vanadium (V) by nano-hydrous zirconium oxide-modified anion exchange resin," *Journal of Hazardous Materials*, vol. 24, article 121386, 2019.

[12] S. Lin, L. Liu, Y. Yang, W. Zhang, C. Lian, and K. F. Lin, "Comparison of the adsorption preference using superparamagnetic Fe_3O_4-SH nanoparticles to remove aqueous heavy metal contaminants," *Chemical Engineering Research and Design*, vol. 125, pp. 319–327, 2017.

[13] C. Liu and F. C. Xie, "Highly efficient removal of As(III) by Fe-Mn-Ca composites with the synergistic effect of oxidation and adsorption," *Science of the Total Environment*, vol. 777, article 145289, 2021.

[14] L. H. Liu, J. R. Zhao, X. Liu, S. Y. Bai, H. Lin, and D. Q. Wang, "Reduction and removal of As(V) in aqueous solution by biochar derived from nano zero-valent-iron (nZVI) and sewage sludge," *Chemosphere*, vol. 277, article 130273, 2021.

[15] S. C. Lou, B. Liu, Y. Qin, Y. Zeng, W. Q. Zhang, and L. F. Zhang, "Enhanced removal of As(III) and As(V) from water by a novel zirconium-chitosan modified spherical sodium alginate composite," *International Journal of Biological Macromolecules*, vol. 176, pp. 304–314, 2021.

[16] H. Mondal, M. Karmaker, N. N. Ghosh, D. K. Maiti, P. K. Chattopadhyay, and N. R. Singha, "One-pot synthesis of sodium alginate-grafted-terpolymer hydrogel for As(III) and V(V) removal: in situ anchored comonomer and DFT studies on structures," *Journal of Environmental Management*, vol. 294, article 112932, 2021.

[17] Y. Qu, L. Qin, X. G. Liu, and Y. Z. Yang, "Magnetic Fe_3O_4/ZIF-8 composite as an effective and recyclable adsorbent for phenol adsorption from wastewater," *Separation Purification Technology*, vol. 294, article 121169, 2022.

[18] N. T. Kiran, "Tailoring the electrical transport properties of ferromagnetic $MnFe_2O_4$ nanoferrite by graphene oxide: an experimental study," *Materials Chemistry and Physics*, vol. 292, article 126844, 2022.

[19] L. T. Thao, T. V. Nguyen, V. Q. Nguyen et al., "Orange G degradation by heterogeneous peroxymonosulfate activation based on magnetic $MnFe_2O_4/\alpha$-MnO_2 hybrid," *Journal of Environmental Sciences*, vol. 124, pp. 379–396, 2023.

[20] G. Q. Yuan, K. Z. Li, J. Z. Zhang et al., "Myrica rubra-like $MnFe_2O_4$ microsphere: a high efficiency microwave reduction catalyst for Cr(VI) removal from water," *Separation and Purification Technology*, vol. 286, article 120434, 2022.

[21] Y. H. Zhan, Y. Y. Meng, Z. X. Xie, and Z. J. Wei, "Synthesis of chitosan/$MnFe_2O_4$@reduced graphene oxide aerogel with radial passageway and its application in removing methylene blue from water," *Functional Materials Letters*, vol. 15, no. 2, p. 2251019, 2022.

[22] B. Zhang, M. Mei, K. W. Li et al., "One-pot synthesis of $MnFe_2O_4$ functionalized magnetic biochar by the sol-gel pyrolysis method for diclofenac sodium removal," *Journal of Cleaner Production*, vol. 381, article 135210, 2022.

[23] Z. Y. Cheng, S. Y. Luo, X. J. Li et al., "Ultrasound-assisted heterogeneous Fenton-like process for methylene blue removal using magnetic $MnFe_2O_4$/biochar nanocomposite," *Applied Surface Science*, vol. 566, article 150654, 2021.

[24] S. Y. Lee, H. Kim, H. Jang et al., "Fabrication of manganese ferrite ($MnFe_2O_4$) microsphere-coated magnetic biochar composite for antimonate sequestration: characterization, adsorption behavior, and mechanistic understanding," *Applied Surface Science*, vol. 578, article 152005, 2022.

[25] W. Ahmed, S. Mehmood, A. N. Delgado et al., "Utilization of Citrullus lanatus L. seeds to synthesize a novel $MnFe_2O_4$-biochar adsorbent for the removal of U(VI) from wastewater: insights and comparison between modified and raw biochar," *Science of the Total Environment*, vol. 77, article 144955, 2021.

[26] C. D. Raquel, B. B. Ana, F. C. Gustavo et al., "Competitive adsorption and desorption of tetracycline and sulfadiazine in crop soils," *Environmental Research*, vol. 214, no. P1, article 113726, 2022.

[27] J. Wang, Y. C. Liu, W. Q. Yin et al., "Solvent-induced facile synthesis of $MnFe_2O_4$ and the As(V) removal mechanism study," *Journal of Molecular Liquids*, vol. 371, article 120845, 2023.

[28] M. Sajid, M. Mohsin, N. D. Avelino et al., "A green method for removing chromium (VI) from aqueous systems using novel silicon nanoparticles: adsorption and interaction mechanisms," *Environmental Research*, vol. 213, article 113614, 2022.

[29] P. Samiyammal, A. Kokila, A. Pragasan et al., "Adsorption of brilliant green dye onto activated carbon prepared from cashew nut shell by KOH activation: studies on equilibrium isotherm," *Environmental Research*, vol. 212, article 113497, 2022.

[30] X. F. Shi, J. M. Hong, L. Kang et al., "Significant improvement on selectivity and capacity of glycine-modified FeCo-layered double hydroxides in the removal of As (V) from polluted water," *Chemosphere*, vol. 281, article 130943, 2021.

[31] X. F. Shi, J. M. Hong, C. Wang et al., "Preparation of Mg,N-co-doped lignin adsorbents for enhanced selectivity and high adsorption capacity of As(V) from wastewater," *Particuology*, vol. 58, pp. 206–213, 2021.

[32] S. Langergren and B. K. Svenska, "Zur theorie der sogenannten adsorption geloester stoffe," *Veternskapsakad Handlingar*, vol. 24, pp. 1–39, 1898.

[33] Y. S. Ho and G. Mckay, "Pseudo-second order model for sorption processes," *Process Biochemistry*, vol. 34, no. 5, pp. 451–465, 1999.

[34] S. Roginsky and Y. Zeldovich, "The catalytic oxidation of carbon monoxide on manganese dioxide," *Acta Physics Chemistry USSR*, vol. 1, p. 554, 1934.

[35] Y. Song, Z. X. Li, S. J. Shao, W. Z. Jiao, and Y. Z. Liu, "High-gravity intensified preparation of D201 resin-hydrated iron oxide nanocomposites for Cr(VI) removal," *Advanced Powder Technology*, vol. 32, no. 5, pp. 1584–1593, 2021.

[36] F. Wang, "Effect of oxygen-containing functional groups on the adsorption of cationic dye by magnetic graphene nanosheets," *Chemical Engineering Research and Design*, vol. 128, pp. 155–161, 2017.

[37] I. Langmuir, "The constitution and fundamental properties of solids and liquids. Part I. Solids," *Journal of the American Chemical Society*, vol. 38, no. 11, pp. 2221–2295, 1916.

[38] H. Freundlich, "Kapillarchemie, eine Darstellung der Chemie der Kolloide undverwandter Gebiete," *Angewandte Chemie*, vol. 36, pp. 91-92, 1923.

[39] M. I. Temkin, "Voprosy Khimicheskoj Kinetiki, Katalisa i React Spos Izd," *Akad Nauk SSSR*, vol. 484, 1955.

[40] K. Narasimharao, L. P. Lingamdinne, S. Al-Thabaiti et al., "Synthesis and characterization of hexagonal Mg-Fe layered double hydroxide/graphene oxide nanocomposite for efficient adsorptive removal of cadmium ion from aqueous solutions: isotherm, kinetic, thermodynamicand mechanism," *Journal of Water Process Engineering*, vol. 47, article 102746, 2022.

[41] L. P. Lingamdinne, V. R. Lebaka, J. R. Koduru, and Y. Y. Chang, "Insights into manganese ferrite anchored graphene oxide to remove Cd(II) and U(VI) via batch and semi-batch columns and its potential antibacterial applications," *Chemosphere*, vol. 310, article 136888, 2023.

[42] Q. F. Wang, T. Chen, P. Bai, J. F. Lyu, and X. H. Guo, "Fe_3O_4-loaded ion exchange resin for chromatographic separation of boron isotopes: experiment and numerical simulation," *Chemical Engineering Research and Design*, vol. 171, pp. 358–366, 2021.

[43] Z. P. Wen, J. B. Xi, J. Lu et al., "Porous biochar-supported $MnFe_2O_4$ magnetic nanocomposite as an excellent adsorbent for simultaneous and effective removal of organic/inorganic arsenic from water," *Journal of Hazardous Materials*, vol. 411, article 124909, 2021.

[44] K. Wojciech, H. Agnieszka, A. Walerian, and M. Ewa, "Adsorption of cationic dyes onto Fe@graphite core–shell magnetic nanocomposite: equilibrium, kinetics and thermodynamics," *Chemical Engineering Research and Design*, vol. 129, pp. 259–270, 2018.

[45] Q. C. Wu, D. F. Wang, C. W. Chen, C. Peng, D. Q. Cai, and Z. Y. Wu, "Fabrication of Fe_3O_4/ZIF-8 nanocomposite for simultaneous removal of copper and arsenic from water/soil/swine urine," *Journal of Environmental Management*, vol. 290, article 112626, 2021.

[46] A. A. Yakout and Z. A. Khan, "High performance Zr-MnO_2@reduced graphene oxide nanocomposite for efficient and simultaneous remediation of arsenates As(V) from environmental water samples," *Journal of Molecular Liquids*, vol. 334, article 116427, 2021.

[47] B. Yan, T. Liang, X. H. Yang, and A. J. Gadgil, "Superior removal of As(III) and As(V) from water with Mn-doped β-FeOOH nanospindles on carbon foam," *Journal of Hazardous Materials*, vol. 418, article 126347, 2021.

[48] S. J. Zeng, D. J. Zhong, Y. L. Xu, and N. B. Zhong, "A novel sulfide-modified nanoscale zero valent iron supported on porous anion exchange resin composite for Cr(VI) effective removal from waste," *Chemical Physics Letters*, vol. 794, article 139494, 2022.

[49] S. P. Zhang, J. Ding, and D. Y. Tian, "Incorporation of MIL-101 (Fe or Al) into chitosan hydrogel adsorbent for phosphate removal: performance and mechanism," *Journal of Solid State Chemistry*, vol. 306, article 122709, 2022.

[50] S. P. Zhang, Y. Y. Dong, Z. Yang, W. B. Yang, J. Q. Wu, and C. Dong, "Adsorption of pharmaceuticals on chitosan-based magnetic composite particles with core-brush topology," *Chemical Engineering Journal*, vol. 304, pp. 325–334, 2016.

[51] S. P. Zhang, Y. Zhang, J. Ding et al., "High phosphate removal using $La(OH)_3$ loaded chitosan based composites and mechanistic study," *Journal of Environmental Sciences*, vol. 106, pp. 105–115, 2021.

[52] C. H. Zhao, L. L. Hu, C. A. Zhang, S. S. Wang, X. Z. Wang, and Z. Y. Huo, "Preparation of biochar-interpenetrated iron-alginate hydrogel as a pH-independent sorbent for removal of Cr(VI) and Pb(II)," *Environmental Pollution*, vol. 287, article 117303, 2021.

[53] S. F. Zhao, Z. S. Li, H. Y. Wang et al., "Effective removal and expedient recovery of As(V) and Cr(VI) from soil by layered double hydroxides coated waste textile," *Separation and Purification Technology*, vol. 263, article 118419, 2021.

[54] C. D. Zhou, C. Y. Han, X. Z. Min, and T. Yang, "Simultaneous adsorption of As(V) and Cr(VI) by zeolite supporting sulfide nanoscale zero-valent iron: competitive reaction, affinity and removal mechanism," *Journal of Molecular Liquids*, vol. 338, article 116619, 2021.

[55] X. B. Zhu, W. Li, S. Tang, M. J. Zeng, P. Y. Bai, and L. J. Chen, "Selective recovery of vanadium and scandium by ion exchange with D201 and solvent extraction using P507 from hydrochloric acid leaching solution of red mud," *Chemosphere*, vol. 175, pp. 365–372, 2017.

[56] T. Peng, Y. S. Si, J. N. Qian et al., "Reduced graphene oxide/$MnFe_2O_4$ nanocomposite papers for fast electrical heating and microwave absorption," *Applied Surface Science*, vol. 613, article 156001, 2023.